CFD simulation of liquid back suction and gas bubble formation in a circular tube with sudden or gradual expansion

Xuan Cai[1], Martin Wörner[2], Holger Marschall[3], Olaf Deutschmann[1,2]

[1]Karlsruhe Institute of Technology (KIT), Institute for Chemical Technology and Polymer Chemistry, Engesserstr. 20, 76131 Karlsruhe, Germany

[2]Karlsruhe Institute of Technology (KIT), Institute of Catalysis Research and Technology, Engesserstr. 20, 76131 Karlsruhe, Germany

[3]Technische Universität Darmstadt, Mathematical Modeling and Analysis, Department of Mathematics, 64287 Darmstadt, Germany

Corresponding Author

Xuan Cai, Karlsruhe Institute of Technology (KIT), Institute for Chemical Technology and Polymer Chemistry, 76131 Karlsruhe, Germany, Tel.: (+49) 721 608 43190, Fax: (+49) 721 608 44805, E-mail: xuan.cai@kit.edu

ORCID of authors

Xuan Cai	0000-0001-9668-2795
Martin Wörner	0000-0003-4630-9292
Holger Marschall	0000-0001-8684-0681
Olaf Deutschmann	0000-0001-9211-7529

Abstract

To avoid potential damage of the dosing unit in selective catalytic reduction by freezing urea-water-solution, the liquid is usually drained from the delivery line when the vehicle is out of operation. When liquid is sucked back counter to the normal delivery direction, the urea-water-solution is replaced by gas with the risk of air being sucked in. In this paper, we study the liquid back suction process and bubble formation numerically by interface-resolving simulations with a phase field method for a generic simplified geometry. We consider two connected circular tubes with sudden or gradual change of the diameter and provide guidelines for proper numerical set-up of such flow problems in order to ensure physically reliable results. We study the influence of the geometry on the liquid draining process through variations of inner and outer tube diameters as well as transition inclination angle. The present numerical results indicate that geometrical modification is an effective means to control liquid draining in expanding pipes while preventing gas bubble formation.

Keywords

Urea-water-solution, SCR, Draining of delivery line, CFD simulation, Phase field method

1 Introduction

Increasingly stringent emission legislations for NO_x require the use of after-treatment technologies, such as the selective catalytic reduction (SCR). In automotive applications, the injection of urea-water-solution (UWS) is a reliable approach for ammonia supply and NO_x reduction [1-8]. Through a pulsed dosing system operating with a controlled duty cycle, the UWS is metered and injected as spray into the exhaust gas flow upstream of the SCR catalyst. There, the droplets evaporate and the urea is decomposed via thermolysis and hydrolysis into ammonia which in turn converts NO_x into harmless nitrogen and water [1,2].

Since the UWS dosing system is a deciding factor for achieving optimal NO_x conversion it is investigated intensively. Birkhold et al. [3,4] performed Lagrangian-particle-tracking simulations of UWS injection to study the spray behavior and its influence on the conversion from the injected UWS to ammonia. The UWS spray process was also investigated experimentally and numerically by Nishioka et al. [9]. Besides, Stola et al. [10] developed a physical model to study UWS supply at system level while Shost et al. [11] employed an embedded model for achieving feedback and control of the UWS dosing system. Meanwhile some innovative dosing strategies were proposed and investigated. Kowatari et al. [12] studied a dosing system assisted with an electrically heated bypass with a hydrolysis catalyst in an effort to enhance NO_x reduction performance at low exhaust gas temperature. Hüthwohl and Dolenec [13] explored a compressed air-support approach for UWS dosing to achieve an optimal atomization resulting in even distribution of the spray. For a detailed overview concerning SCR and UWS dosing technology we refer to the recent book by Nova and Tronconi [8].

During long standstill periods of the delivery unit, the UWS can freeze if the temperature is below about −11°C. Aus der Wiesche [14] and Choi and Woo [15] studied the associated phase change and heat transfer processes in the UWS tank by computational fluid dynamics (CFD). Since UWS expands as it freezes, the corresponding volume expansion in the pump and/or in the delivery line may damage the dosing unit. It is therefore common practice to drain the delivery unit upon cessation of operation of the motor vehicle. Back-suction counter to the normal delivery direction is a particularly advantageous way of draining the delivery unit [16]. Within the draining process, UWS is replaced by air that is sucked in by a supply device. During the back suction, there is a risk of air being sucked into the delivery unit. In particular, gas bubbles may form at any sudden or gradual change of the channel cross-section. Such gas

formation should be prevented, since it will adversely affect the working pressure required for UWS supply to dosing point as well as atomization, which may degrade the efficiency and reliability of the entire dosing system. Eriksson and Carlsson [17] discuss further damages of gas emergence on the dosing unit, such as performance reduction of the cooling system accompanied by an increased risk of over-heating components sensitive to temperature.

In the present contribution, we investigate the UWS draining from the delivery line by interface-resolving simulations of the gas-liquid two-phase flow. To this end, a rather simple but general tubular geometry is considered. It consists of two concentric circular pipes with different diameters that are connected by a truncated cone (Figure 1 a). By CFD simulations, we investigate the influences of the cone angle (α) and of the inner diameters of the smaller (D_1) and larger (D_2) tubes on the back-suction process and potential gas bubble formation. The numerical results indicate that geometrical modification may be an effective method to prevent gas bubble formation. To the best of our knowledge, the present numerical study is the first of its kind for this hydrodynamic problem, at least in the context of SCR.

The numerical simulations are performed with a phase field method. As a diffuse interface method [18], it is particularly suitable for the present investigation where an accurate modeling of the moving three-phase contact line at the inner wall of a tube is required. Recently we implemented a phase field method coupled with the Navier-Stokes equations as a novel top level OpenFOAM® solver *phaseFieldFoam* [19,20]. The code was validated for a variety of wetting-related and capillary-driven interfacial flows such as capillary rise and droplet spreading on solid surfaces [21] and bubble cutting by a solid cylinder [22]. In this study, *phaseFieldFoam* is applied to study the UWS draining and bubble formation for the above pipe system. Furthermore, from the present experiences, guidelines for obtaining reliable CFD results for such flow problems are proposed. These may be useful for future CFD-based design and optimization studies of technical geometries by the community.

The remainder of the paper is organized as follows. In Section 2, we introduce the phase field method in terms of its mathematical formulation and numerical implementation. In Section 3 we present the numerical setup and test cases. The numerical results concerning computational issues and different geometries are presented and discussed in Section 4. In Section 5, conclusions and an outlook are given.

2 Phase Field Method

The phase field method is a diffuse interface method and treats the interface as a thin transition layer of finite width [23]. This is in contrast to other interface-capturing methods such as the level-set method and geometric volume-of-fluid method where the interface width is zero (sharp-interface). It is also distinct from algebraic volume-of-fluid methods (on which the standard OpenFOAM® solver *interFoam* [24] is based) where the interface is conceptually sharp but numerically diffuse (for an overview on the various methods, see, e.g., [25]). The phase field method endowed with physically diffuse interface dates back to van der Waal's insight that the interface in reality is diffuse with a certain mixing between two phases [26]. While the thickness of a real interface is on the nanometer scale, the length scales of the present flow phenomena are roughly six orders-of-magnitude larger. This huge disparity between the two length scales poses a prohibitive computational cost if a diffuse interface of real physical thickness is considered in the simulation and adequately resolved. For feasible phase field simulations of interfacial flows, an artificially thickened interface is adopted and the model parameters should be chosen to scale appropriately and set accordingly such that macroscopic interfacial dynamics are accurately recovered. Therefore, in addition to the governing equations and numerical implementation, a practical strategy for choosing the model parameters is presented in this section.

2.1 Cahn-Hilliard-Navier-Stokes Equations

In the phase field method, the spatial distribution and time evolution of the liquid (L) and gas (G) phases are described by an order parameter (C), also denoted as phase field variable. Here, C takes distinct values $C_L = 1$ and $C_G = -1$ in the liquid and gas bulk phases and varies rapidly yet smoothly in a thin transition layer (i.e., the diffuse interface). The interface dynamics is governed by the convective Cahn-Hilliard equation

$$\frac{\partial C}{\partial t} + (\mathbf{u} \cdot \nabla) C = M \nabla^2 \phi \tag{1}$$

where t denotes time, $\mathbf{u}$ the velocity field and M is the Cahn-Hilliard mobility parameter. The chemical potential ϕ consists of a bulk and interface contribution

$$\phi = \frac{\lambda}{\varepsilon^2} C(C^2 - 1) - \lambda \nabla^2 C \tag{2}$$

Here, ε is a positive constant (denoted as capillary width) which determines the thickness of the diffuse interface (see Section 2.3). For an equilibrium system, the capillary width and the mixing energy density λ relate to the interfacial tension as [27,28]

$$\lambda = \frac{3\sqrt{2}\sigma\varepsilon}{4} \tag{3}$$

The term on the right hand side of Eq. (1) provides a diffusive mechanism for motion of the contact line at a no-slip wall. Based on the wall free energy formulation at local equilibrium, one can derive the following boundary condition to account for the wettability of the solid substrate [29]

$$\mathbf{n}_s \cdot \nabla C = \frac{\sqrt{2}}{2}\frac{\cos\theta_e}{\varepsilon}(1 - C^2) \tag{4}$$

Here, θ_e is the equilibrium contact angle and $\mathbf{n}_s$ is the outward unit normal to the solid surface. Recent phase field computations [28,30] employing this energy equilibrium boundary condition showed a recovery of the hydrodynamic wetting theory of Cox [31], which can be regarded as a representative dynamic contact angle model. In the present computations, the capillary number based on the contact line velocity U_{cl} is very small, typically $Ca_{cl} = \mu_L U_{cl} / \sigma \approx 10^{-3} - 10^{-4}$. Thus, the difference between dynamic contact angle and equilibrium contact angle is expected to be small as well.

In this study, we consider two-phase flows consisting of two immiscible, incompressible, isothermal and Newtonian fluids. Thus, the flow can be described by a solenoidal condition for the velocity field, Eq. (5), and the single-field Navier-Stokes equations (6)

$$\nabla \cdot \mathbf{u} = 0 \tag{5}$$

$$\frac{\partial}{\partial t}(\rho_C \mathbf{u}) + \nabla \cdot (\rho_C \mathbf{u} \otimes \mathbf{u}) = -\nabla p + \nabla \cdot \left[\mu_C \left(\nabla \mathbf{u} + (\nabla \mathbf{u})^T \right) \right] + \mathbf{f}_\sigma + \rho_C \mathbf{g} \tag{6}$$

where p is the pressure and $\mathbf{g}$ the gravity vector. For the surface tension term $\mathbf{f}_\sigma$, two formulations can be roughly found in literature: one based on a continuum surface force [32] and the other formed with a chemical potential [23]. He and Kasagi showed that the latter outperforms the former with respect to the huge reduction of parasitic flows [33]. Therefore, we use the chemical potential-based surface tension formulation

$$\mathbf{f}_\sigma = -C \nabla \phi \tag{7}$$

The density and viscosity fields depend on the order parameter as

$$\rho_C = \frac{1+C}{2}\rho_{\mathrm{L}} + \frac{1-C}{2}\rho_{\mathrm{G}} \quad \text{and} \quad \mu_C = \frac{1+C}{2}\mu_{\mathrm{L}} + \frac{1-C}{2}\mu_{\mathrm{G}} \tag{8}$$

where $\rho_{\mathrm{L/G}}$ and $\mu_{\mathrm{L/G}}$ denote the density and viscosity of the phases. Through Eqs. (7) and (8) and the common velocity field, the Navier-Stokes Eq. (6) and the Cahn-Hilliard Eq. (1) are coupled with each other.

2.2 Numerical Implementation and Solution Procedure

The above system of equations is implemented in the platform of foam-extend, a community-driven fork and adaptation of the open-source CFD software OpenFOAM® [34]. Concerning the solution procedure for the Cahn-Hilliard equation within a single time-step, *phaseFieldFoam* offers two alternatives: segregated and coupled. With the here-adopted segregated method, the solution procedure from time step n to $n + 1$ is as follows:

(1) Solve the Cahn-Hilliard equation (1) to gain the order parameter field at time-step $n + 1$.
(2) Calculate the chemical potential, see Eq. (2), with updated order parameter field.
(3) Calculate the surface tension, mixture-density and -viscosity, see Eq. (7) and Eq. (8).
(4) Solve the Navier-Stokes equations, see Eq. (5) and Eq. (6), to obtain the velocity field at time-step $n + 1$.

The code *phaseFieldFoam* is equipped with state-of-the-art numerical techniques for computational boundedness, mass conservation and numerical efficiency. Similar to Ding et al. [35] and Abels et al. [36], a relative density flux due to diffusion of two phases is inserted into the Navier-Stokes equation to guarantee mass conservation for two-phase flows with a large density contrast. Moreover, as long as the segregated solution is in use, a temporal sub-cycling is employed; therewith the Cahn-Hilliard equation is solved more than one time within a single time-step to improve convergence of the solution. This feature is alike to the solution strategy for the volume fraction equation in the standard OpenFOAM® solver *interFoam* [37]. Further details concerning *phaseFieldFoam* can be found in Marschall et al. [19,20].

In all present simulations, the following numerical schemes are used. Spatial derivatives are approximated by a high-resolution scheme (Gauss Gamma) and time integration is handled by a second order two-time level backward scheme. The time step is adapted during simulations; therein the maximum Courant number is set to 0.1. The order of magnitude of the time step is typically 10 μs.

2.3 Model Parameters

Considering the diffuse interface representation of the phase field method, using a mesh that adequately resolves the interfacial transition region is critical for obtaining reliable simulation results. For a planar interface at equilibrium, the solution of Eq. (1) yields a hyperbolic tangent profile for the order parameter $C = \tanh(x/\sqrt{2}\varepsilon)$, where x is the coordinate normal to the interface. It is common practice to define L_C as the distance from $C = -0.9$ to $C = 0.9$, so that one obtains $L_C = 2\sqrt{2}\varepsilon \tanh^{-1}(0.9) = 4.164\varepsilon \approx 4\varepsilon$ [23]. To quantify the grid resolution of the diffuse interface, we define a parameter $N_C = L_C / h \approx 4\ \varepsilon / h$ where h is the mesh width. In Section 4.1.4, a mesh-independence study will be performed through variation of h and N_C.

In the governing equations presented in Section 2.1, there are three phase field specific parameters (ε, M and λ). With a given surface tension, λ can be determined through Eq. (3). Therewith only ε and M need to be fixed. However, choosing appropriate values for a certain flow problem is rather tricky, since it is almost impossible to measure these parameters in experiments. Therefore, we follow a pragmatic approach for selecting appropriate values for ε and M.

The value of the capillary width ε is selected relative to a characteristic macroscopic length scale of the flow problem, here the inner diameter of the smaller tube (D_1). To quantify the ratio of both length scales, the Cahn number is defined as $Cn = \varepsilon / D_1$. From the experiences of the authors [21,22] as well as of other researchers [29,38], we suggest that ε is chosen such that $Cn \leq 0.01 \sim 0.02$, then the simulated interfacial flow phenomena get rather insensitive to ε.

The mobility M quantifies a diffusion process that governs the motion of the contact line. The characteristic length scale of this diffusion process is of nanometer scale and its resolution is beyond any computational capacities. Thus, we treat M as a phenomenological parameter. For choosing a suitable value of M, the following procedure is adopted. Firstly, by following the relation $M = O(\varepsilon^2)$ a rough value for the mobility parameter is estimated. As demonstrated by Jacqmin [23], through this relation a sharp interface limit can be properly approached as ε goes to zero; a non-dimensional form of this relation was also adopted by Ding et al. [39]. Around this preliminary estimate, M is then fixed by fitting with, if available, experimental/analytical data, since M can be regarded as a material intrinsic property of a certain physical system [40].

3 Computational Setup and Test Cases

3.1 Geometry

Figure 1 a) shows a sketch of the considered generalized channel geometry. While the values of the pipe diameters D_1 and D_2 and that of the inclination angle α are variable, the heights are fixed here to H_1 = 10 mm and H_2 = 30 mm, respectively. In this paper, six principal geometrical variants (V1-V6) as listed in Table 1 are investigated, where the diameter ratio D_2 / D_1 is in the range 1.3 – 2. In addition, one case with α = 90° is considered (V0) where the diameter ratio is increased to 5. It resembles bubble formation at a single submerged orifice and serves for comparison and validation. For the case of a sudden expansion (α = 90°) the prominent role of the diameter ratio D_2 / D_1 is intuitively evident, as for very large values bubbles will form whereas no bubble formation is to be expected for capillary tubes with diameter ratio approaching unity.

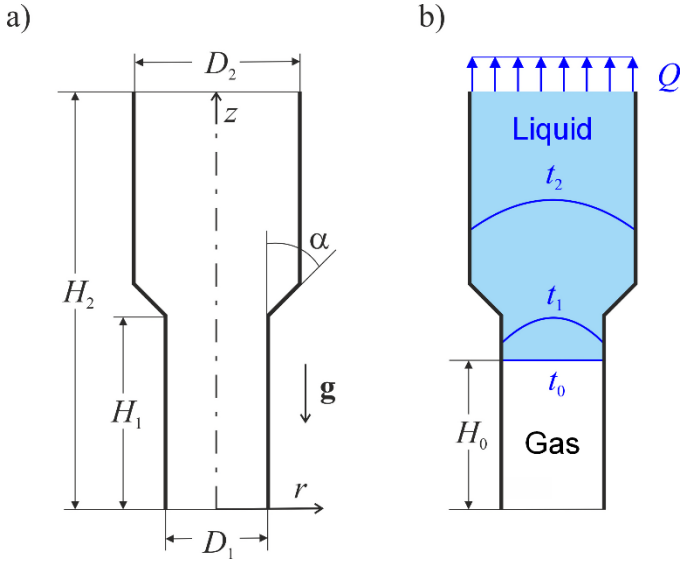

Figure 1: (a) Schematic of a general channel geometry with variable cross-section. The concentric circular tubes (inner diameters D_1 and D_2) are connected by a truncated cone (inclination angle α). (b) Sketch of liquid back suction process, with retracting gas-liquid interface for different instants in time (t_0 = initial interface position, $t_2 > t_1 > t_0$)

Table 1: Parameters of geometrical variants

Variant	D_1 [mm]	D_2 [mm]	D_2 / D_1 [–]	α [°]
V0	4	20	5	90
V1	4	6	1.5	90
V2	3	4	$1.\overline{3}$	90
V3	3	6	2	90
V4	3	6	2	35
V5	3	6	2	50
V6	3	6	2	55

Surprisingly, it seems that liquid withdrawal from an expanding pipe has not been investigated so far; the authors at least were unable to identify related studies in literature. However, a similar geometry as sketched in Figure 1 is considered in several analytical [41-43] and numerical [44-46] studies on capillary suction in micropores where liquid is drawn by capillary forces from the larger into the smaller pore (wicking flow). In the present study in contrast, the pipe diameter is in the order of millimeters not micrometers and the flow is pressure driven opposing to capillary forces for $\theta_e < 90°$.

3.2 Boundary & Initial Conditions and Mesh

In this paper, two-dimensional (2D) axisymmetric simulations as well as three-dimensional (3D) simulations are performed. For 2D axisymmetric simulations, the computational domain is a wedge discretized by a uniform grid (Figure 2). The boundary conditions applied for the velocity, pressure and order parameter at the various boundary patches are given in Table 2. In the phase field method, the contact angle of the three-phase contact line is incorporated into the boundary condition for the order parameter, cf. Eq. (4). For obtaining reliable simulation results, therefore, the mesh quality close the solid wall is of special relevance. For variants with $\alpha <$ 90°, the truncated cone region is therefore meshed with an aligned grid (Figure 2 c).

For the 3D simulations, a 90° segment is considered in combination with symmetry boundary conditions at the lateral faces (Figure 3 a). The boundary conditions at the other patches are identical with those listed in Table 2. Figure 3 c) and d) show cross-sections of two

meshes that have about the same resolution (h = 80 µm) but are created with different mesh generators. The main difference is that the mesh in Figure 3 c) is aligned at the tube wall while that in Figure 3 d) is non-aligned.

In all simulations, both phases are initially stagnant. At the top outlet of the computational domain, a uniform outlet velocity corresponding to a fixed liquid volumetric flow rate Q = 700 mm^3/s is specified. The corresponding liquid velocities at the outlet are 55.7 mm/s for case V2, 2.2 mm/s for case V0, and 24.8 mm/s for all other cases. In all simulations, the interface is initially flat and located at position H_0 = 9 mm (Figure 1 b). A comparison with one simulation using a smaller value of H_0 showed identical results for the draining process.

Table 2: Boundary conditions at the various patches

Patch	velocity	pressure	order parameter
inlet	zero gradient	zero relative pressure	$C = -1$
outlet	uniform velocity	zero gradient	inletOutlet
tube wall	zero	zero gradient	Eq. (4)

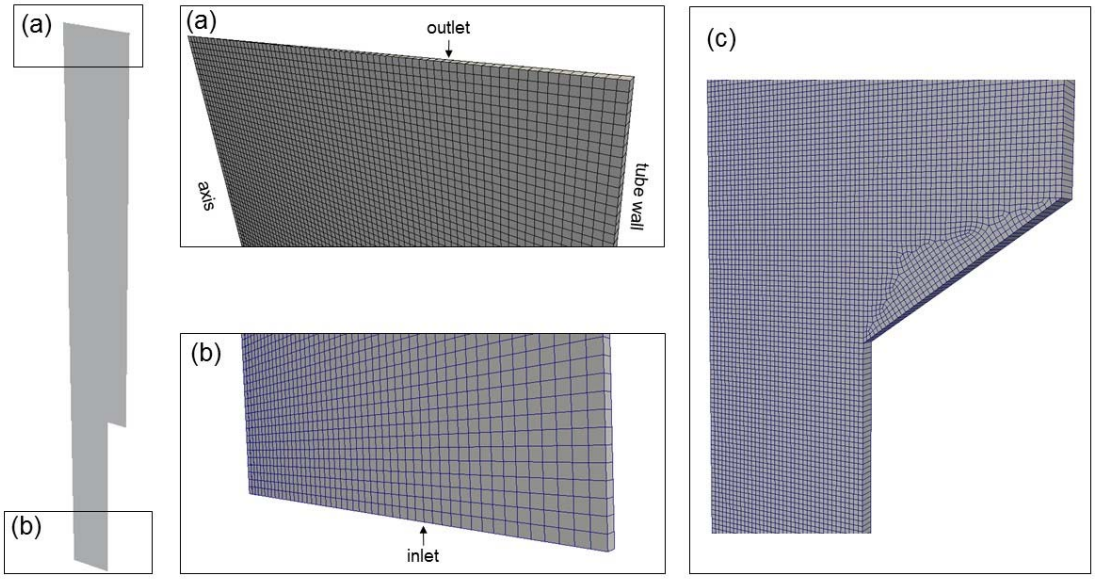

Figure 2: Wedge-type computational domain for 2D axisymmetric simulations ($\alpha = 90°$). The close-up views show the mesh at the top (a) and bottom (b) with boundary patches. For variants with $\alpha < 90°$ the truncated cone region is meshed by an aligned grid (c)

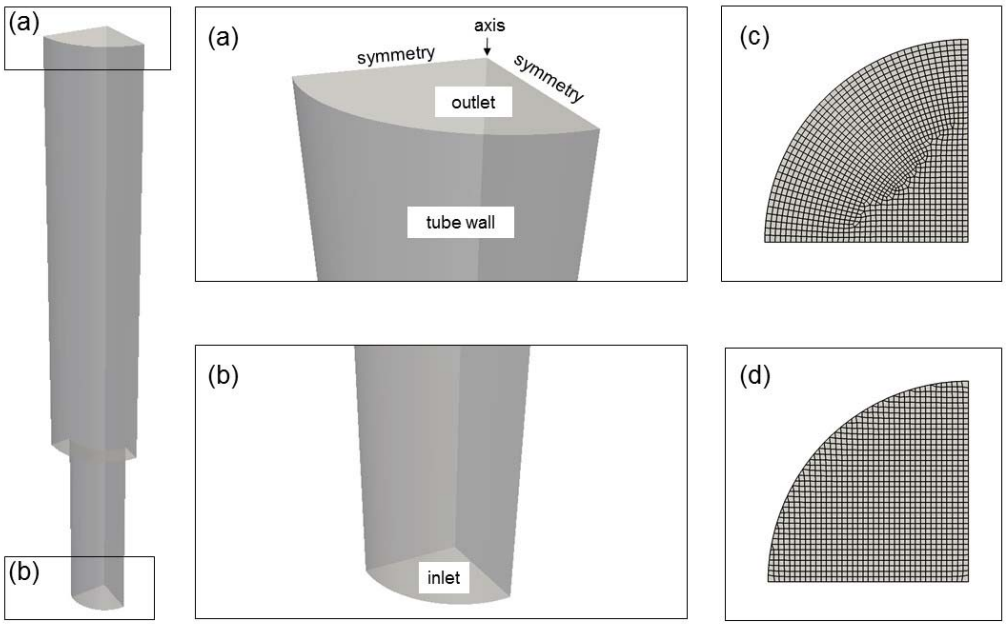

Figure 3: One-quarter cylindrical geometry for 3D simulations ($\alpha = 90°$). The close-up views show the top (a) and bottom (b) of the domain with boundary patches and a top view on meshes with (c) and without (d) alignment near the tube wall

3.3 Fluid Properties

All simulations are performed with constant UWS-representative fluid properties as follows: liquid density $\rho_L = 1080$ kg/m^3, gas density $\rho_G = 1$ kg/m^3, liquid viscosity $\mu_L = 1.296\times10^{-3}$ Pa·s, gas viscosity $\mu_G = 1.48\times10^{-5}$ Pa·s, surface tension coefficient $\sigma = 0.073$ N/m, equilibrium contact angle $\theta_e = 55°$. The gravity vector points in negative z-direction with gravitational acceleration $g = 9.81$ m/s^2.

4 Results and Discussion

In this section, we first present the numerical studies concerning computational issues, namely, simulation dimensionality, mesh quality and resolution as well as mobility parameter. For this purpose, the baseline case V1 with D_1 = 4 mm, D_2 = 6 mm and α = 90° is considered. The corresponding results are presented in Section 4.1. From these investigations, suitable numerical parameters are identified and used for the further simulations. In Section 4.2, we study the influences of the geometry on liquid draining and the gas bubble formation process through variation of D_1, D_2 and α. In the analysis of the results we focus on the temporal evolution of the interface which is visualized as the set of locations where $C = 0$.

4.1 Parametric Studies on Computational Issues

4.1.1 Influence of Mesh Quality in 3D simulations

To study the influence of mesh quality, 3D simulations are performed for both meshes displayed in Figure 3 c) and d) using the same parameter setup (ε = 80 µm, Cn = 0.02, $M = 48\times10^{-10}$ m^3s/kg, N_C = 4). Figure 4 compares snapshots of the interface obtained on both meshes for different instants in time. In the initial stage of the simulations (e.g. for t = 0.12 s and t = 0.28 s) the results of both meshes are almost identical and rotationally symmetric (Figure 4 a, b, e, f). The results obtained with the wall-aligned mesh stay rotationally symmetric in the later stage of the simulation and there is always a thin liquid film between the bubble and the wall (Figure 4 c, d). However, the results for the mesh without wall alignment deviate from rotational symmetry for t = 0.35 s (Figure 4 g). Furthermore, for this instant in time a gas plug has formed which is in direct contact with the wall of the larger upper tube. During the course of this simulation, the distorted interface relaxes to a rotationally symmetric form (t = 0.38 s) and the gas plug rises in contact with the wall while there is no liquid film (Figure 4 h).

This comparison shows that the numerical results depend significantly on the mesh topology. Clearly, the deviation from rotational symmetry in Figure 4 g) is not physical but rather a numerical artefact. Obviously, this artefact is related to the non-orthogonal grid close to the wall (cf. Figure 3 d). This leads to an inaccurate computation of the wall boundary condition for the order parameter (cf. Eq. (4)), which triggers the numerical instability leading to a temporary deviation from rotational symmetry.

To improve the computation of gradients at the wall on distorted grids, OpenFOAM® offers an option for surface normal gradient correction for non-orthogonality. This option is switched on through setting *snGradSchemes* to *corrected* in the file *system/fvSchemes* (refer to Chapter 4 in the OpenFOAM® User Guide [37]). Phase field simulations with this non-orthogonality correction (not shown here) yield rotationally symmetric results for the non-aligned mesh in Figure 3 d) that are identical with those obtained on the aligned mesh in Figure 3 c). However, further test simulations have shown that even with this gradient correction, non-axisymmetric unphysical results may be obtained on the non-aligned mesh, if M is decreased below a certain critical value. It thus turned out that obtaining rotationally symmetric solutions in 3D phase field simulations for physically axisymmetric problem is not trivial. Here, the use of an orthogonal grid close to the wall and of the mentioned correction options are essential.

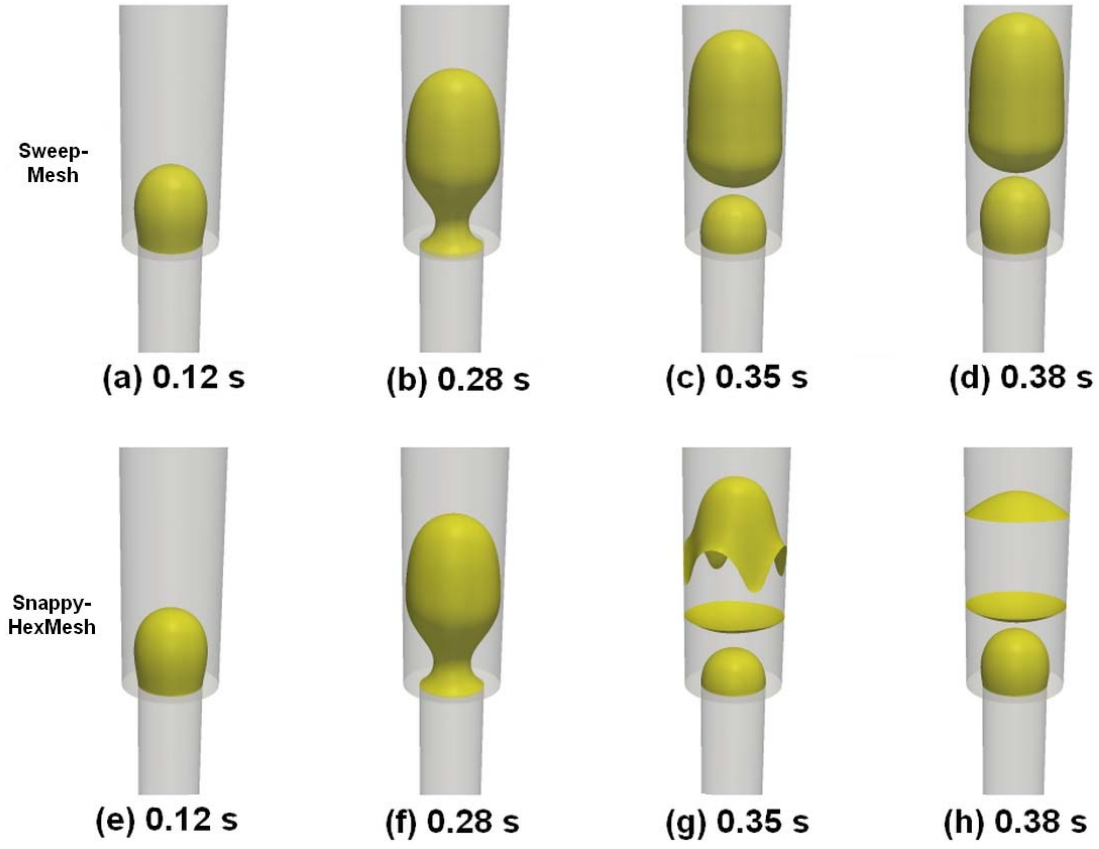

Figure 4: Influence of mesh type on temporal evolution of gas-liquid interface (yellow iso-surface $C = 0$). Upper row: results obtained with the wall-aligned mesh from Figure 3 c), lower row: results obtained with the non-aligned mesh from Figure 3 d)

4.1.2 Mass Conservation and Liquid Inventory

An important issue in interface-resolving numerical simulation of gas-liquid flows is mass conservation. When homogenous Neumann boundary conditions are employed at all domain boundaries, the phase field method conserves the order parameter globally, but not the volume of disperse bubbles or drops which tend to shrink or expand [47]. For the present test problem, neither the liquid nor the gas volume within the computational domain is constant in time. Accessing mass conservation in the simulation is thus intricate.

Given the constant liquid flow rate Q = 700 mm^3/s specified via a uniform velocity over the outlet cross-section, the linear relationship $V_{\mathrm{L}} = V_{\mathrm{L},0} - Q \cdot t$ should hold for the instantaneous liquid volume within the computational domain. Here $V_{\mathrm{L},0}$ denotes the initial liquid volume, which is 578 mm^3 for case V1 in Figure 4. Evaluating the liquid volume within the computational domain for the simulation displayed in Figure 4 a-d) yields a linear relation as well, but with slightly different slope corresponding to a reduced effective liquid outflow rate of about 614 mm^3/s. While this discrepancy appears quite large, it can be attributed to the fact that in the simulation both phases are initially stagnant except at the outlet boundary where an unphysical velocity discontinuity occurs at t = 0 s. Consequently, physical velocity profiles in both bulk phases need to develop over time, which occurs delayed, e.g., due to liquid inertia. A computational set-up where initial and outlet boundary conditions match more appropriately from a physical point of view would thus be required for accessing mass conservation in greater detail, a topic that is not further investigated here.

4.1.3 2D versus 3D Simulations

In this study a lineup of parametric investigations are to be carried out. To save computational time, 2D axisymmetric simulations are typically preferred. Therefore, the use of 2D axisymmetric simulations needs to be justified. It is carried out through the comparison of the 3D simulation reported in Section 4.1.1 with 2D axisymmetric simulation using the same parameter setup (h = 40 µm, ε = 80 µm, Cn = 0.02, N_{C} = 4, M = 48×10^{-10} m^{3}s/kg). As shown in Figure 5, identical numerical results are achieved in comparison with those from the 3D simulation. Hence, all subsequent simulations are performed with the 2D axisymmetric setup.

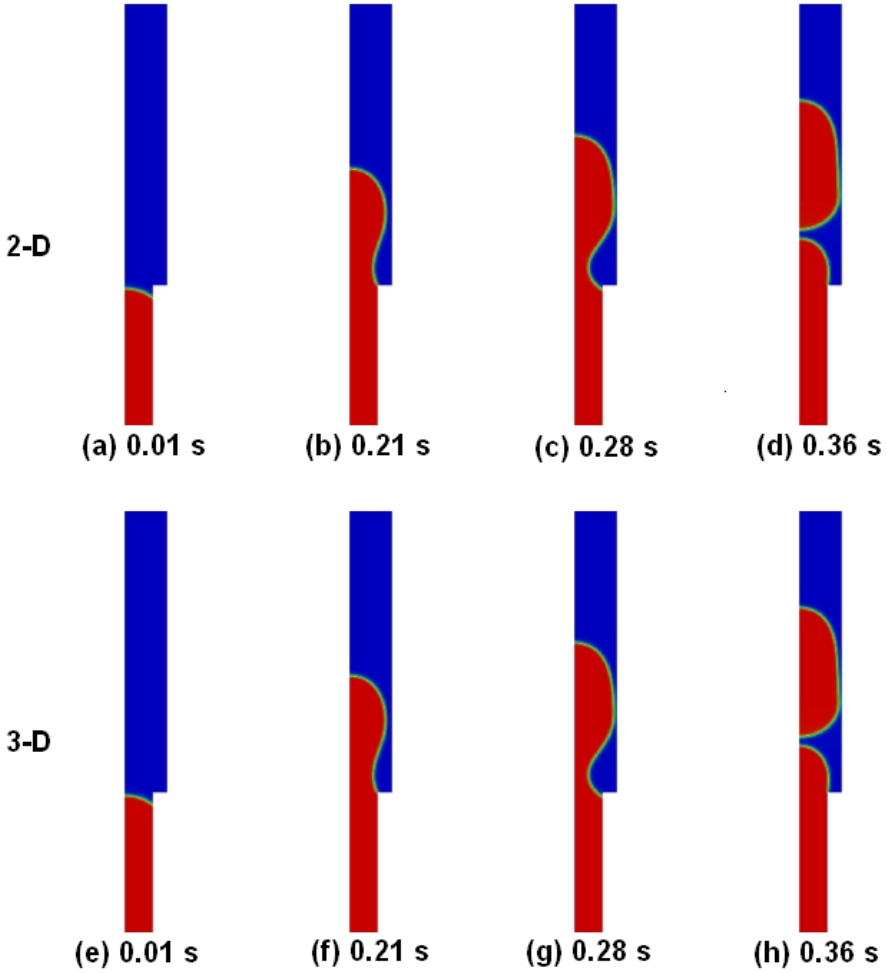

Figure 5: Time evolution of phase distribution (blue = liquid, red = gas) in 2D axisymmetric simulation (top) and 3D simulation (bottom, vertical cut) (variant V1, h = 40 µm)

4.1.4 Mesh-independence Study

For reliable and trustworthy computational studies, it is essential to obtain grid-independent results. We carry out simulations for three different resolutions (h = 40, 30, 20 µm) with fixed values of capillary width (ε = 40 µm, Cn = 0.01) and mobility (M = 16×10^{-10} m^3s/kg). The results for these three progressively refined meshes are qualitatively compared in Figure 6. All mesh resolutions produce the same results for the first stage of liquid draining (Figure 6 a, e, i) and bubble growth (Figure 6 b, f, j). Differences occur during the short period before gas pinch-off (Figure 6 c, g, k). The simulations on the mesh with N_C = 6 and 8 predict almost the same time instant for pinch-off (Figure 6 h and l), while N_C = 4 will give a later instant (Figure 6 d).

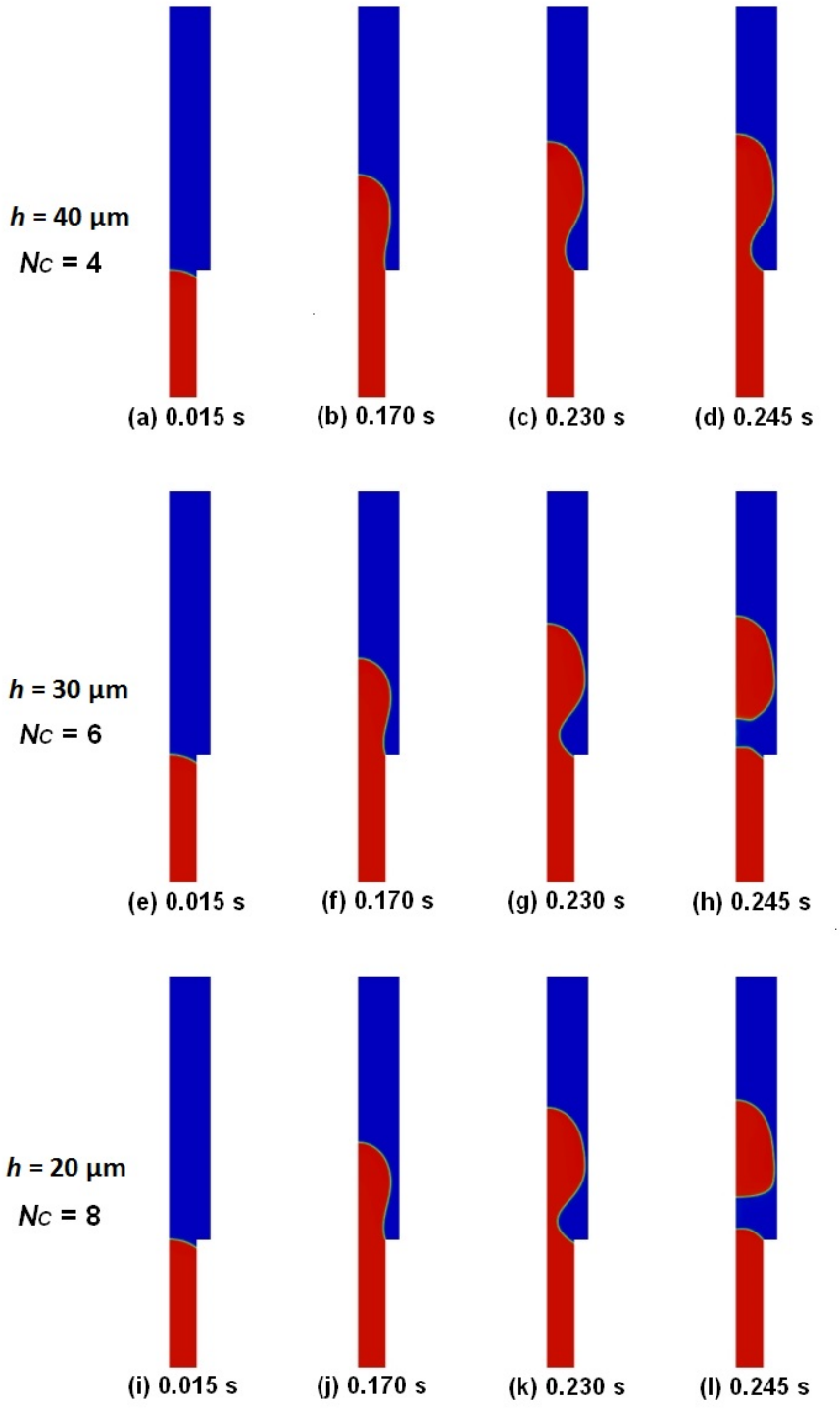

Figure 6: Influence of mesh resolution on temporal evolution of phase distribution (variant V1, 2D axisymmetric simulations, $\varepsilon = 40$ µm, $Cn = 0.01$, $M = 16\times10^{-10}$ m^{3}s/kg)

To compare the computational results on different grids quantitatively, two geometrical quantities are defined to characterize the interface evolution: gas phase height (H) and minimum liquid film thickness (δ_F), as shown in Figure 7. The temporal evolution of H and δ_F is exhibited in Figure 8 and Figure 9, respectively. Both figures indicate that the simulation results become grid-independent when the length L_C is resolved by at least six mesh cells ($N_C \geq 6$). In this case, the terminal value of the liquid film thickness is $\delta_F = 167$ µm. This film thickness is resolved by about five mesh cells for the case with $h = 30$ µm and $N_C = 6$.

In a theoretical investigation for a semi-infinite bubble, Bretherton [48] derived the following relation between the capillary number $Ca_B = \mu_L U_B / \sigma$ and the liquid film thickness:

$$\delta_F = \frac{D}{2} \cdot 1.3375 \cdot Ca_B^{2/3} \tag{9}$$

This correlation is approximately valid for very long Taylor bubbles moving in straight circular tubes of constant cross-section with a constant bubble velocity U_B corresponding to $Ca_B \leq 3\times10^{-3}$. For the bubble in Figure 6 d) it is $U_B \approx 33$ mm/s which corresponds to $Ca_B = 5.8\times10^{-4}$. For this value, Eq. (9) predicts a film thickness of $\delta_F = 2.5$ µm which is about 67 times smaller than in the present case. This suggests that Bretherton's correlation for the liquid film thickness is (not surprisingly) not valid here, where the pipe diameter is suddenly expanding, the bubble formed is rather short and the flow is not fully developed.

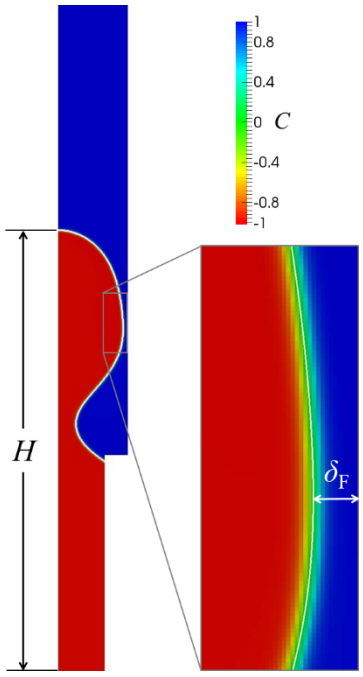

Figure 7: Schematic of gas height (H) and minimum liquid film thickness (δ_F)

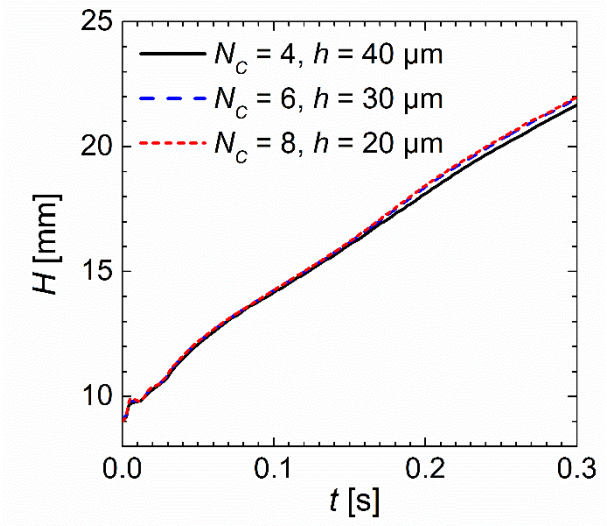

Figure 8: Influence of grid size on temporal evolution of gas height (variant V1, 2D axisymmetric simulations, $\varepsilon = 40$ µm, $Cn = 0.01$, $M = 16\times10^{-10}$ m^{3}s/kg)

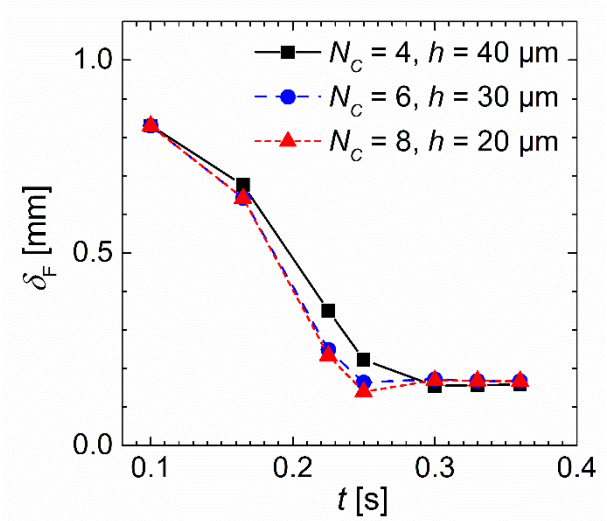

Figure 9: Influence of grid size on temporal evolution of minimum liquid film thickness (variant V1, 2D axisymmetric simulations, $\varepsilon = 40$ µm, $Cn = 0.01$, $M = 16\times10^{-10}$ m^{3}s/kg)

4.1.5 Mobility Parameter

Following the relation $M = O(\varepsilon^2)$ discussed in Section 2.3, a rough range for the mobility parameter M is determined. Within this range, three values (M = 16×, 8× and 4×10^{-10} m^3s/kg) are selected to study the mobility influence on the bubble formation process. Apart from varying M, all other numerical parameters are fixed (h = 30 μm, ε = 40 μm, Cn = 0.01, N_C = 6). The results are displayed in Figure 10. For the first stage of gas rise and bubble growth, computational results are insensitive to the choice of M (Figure 10 a, e, i, b, f, j). At the later stages, when gas pinch-off arises, the simulation with a larger M predicts an earlier time instant for occurrence of pinch-off (Figure 10 k). Here, no experimental data is available so that no optimal value of M can be fixed for the present flow system. In recent simulations with a phase field method, Bai et al. [49] show that the drop pinch-off process in a liquid-liquid two-phase flow through a flow focusing microfluidic channel is influenced by the mobility. Suitable values for M are then determined by matching of the computational results with experiments.

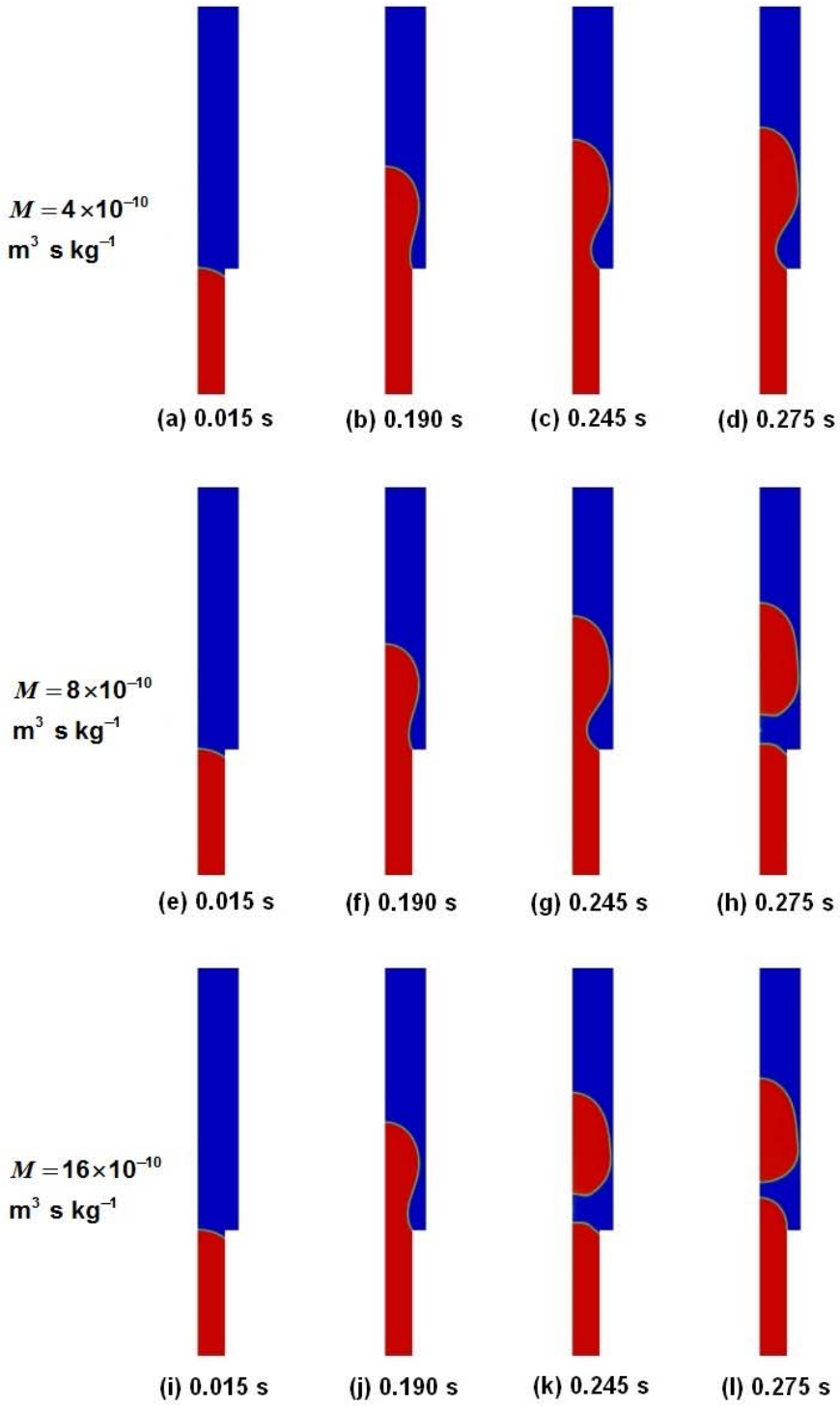

Figure 10: Influence of mobility (M) on time evolution of phase distribution (variant V1, 2D axisymmetric simulations, h = 30 µm, ε = 40 µm, Cn = 0.01, N_C = 6)

4.2 Parametric Studies on Tube Geometry

This section is devoted to investigation into the influence of the tube geometry on the liquid draining and bubble formation process. Three different aspects are studied. First, a comparison of bubble formation under confined and unconfined conditions is performed. Second and third, the effects of the tube diameters and the influence of the inclination angle are studied for confined conditions.

4.2.1 Wall Effect on Bubble Formation

To study the effect of the upper pipe wall on the bubble formation process, simulation results for variant V1 with diameter ratio $D_2 / D_1 = 1.5$ are compared with case V0 where the diameter ratio is increased to 5. Figure 11 shows the temporal evolution of the gas-liquid interface for both cases for six different instants in time. Until $t = 0.19$ s the bubble formation is not affected by the upper pipe wall. Slightly later, at $t = 0.205$ s the neck for case V0 is already notably thinner as compared to variant V1. At $t = 0.225$ s the bubble is pinched-off and has risen a certain distance for case V0, whereas for case V1 the pinch-off occurs delayed. For case V0, the shape of the bubble is approximately ellipsoidal and oscillating as the bubble rises (Figure 11 e, f). For case V1 instead, the pinched-off gas forms a Taylor bubble due to the confinement by the upper pipe wall (Figure 11 l).

Case V0 approaches the bubble formation from a single submerged orifice into an unconfined stagnant liquid. The latter topic has been investigated comprehensively and various correlations exist in literature relating the bubble volume to hydrodynamic parameters. Here, we use a correlation for constant gas flow rate [50] in the form as given in [51]

$$\frac{V_\mathrm{B}}{R_\mathrm{I}^3} = \frac{4\pi}{3}\left(\frac{1.119}{Bo^{1.08}} + 1.406\frac{Fr^{0.36}}{Ga^{0.39}} + 0.469 Fr^{0.51} \right) \tag{10}$$

where $Bo = \rho_\mathrm{L} g R_\mathrm{I}^2 / \sigma$ denotes the Bond number, $Fr = Q^2 / R_\mathrm{I}^5 g$ the Froude number and $Ga = \rho_\mathrm{L}^2 R_\mathrm{I}^3 g / \mu_\mathrm{L}^2$ the Galileo number. Here, these dimensionless numbers take the values $Bo = 0.58$, $Fr = 1.56$ and $Ga = 5.45 \cdot 10^4$, corresponding to a bubble volume of 88 mm^3 according to Eq. (10). The volume of the pinched-off bubble in Figure 11 e) is 106 mm^3. This corresponds to an overestimation of about 20% in the simulation as compared to the correlation, which seems quite acceptable considering the presence of sidewalls and the non-zero mean liquid velocity in the simulation.

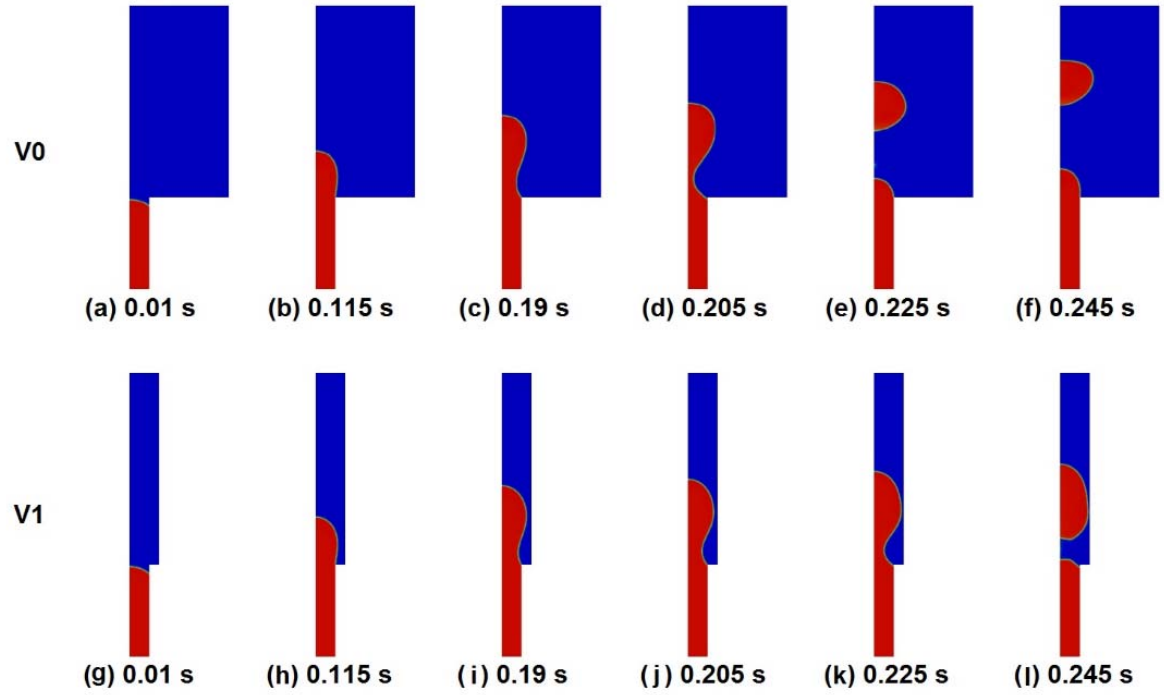

Figure 11: Influence of upper pipe-wall on bubble formation ($D_1 = 2R_1 = 4$ mm, variants V0 and V1, 2D axisymmetric simulations, $h = 30$ µm $\varepsilon = 40$ µm, $N_C = 6$, $M = 16\times10^{-10}$ m^{3}s/kg)

4.2.2 Variation of Tube Diameters

To study the influence of the lower and upper tube diameter on bubble formation under confined conditions, the geometrical variants V1, V2 and V3 are considered (all with $\alpha = 90°$). The computational results are shown in Figure 12. As can be seen, gas pinch-off can be observed for variants V1 and V3 but not for variant V2. This result is at first hand surprising. However, it has its origin in the fixed outlet volumetric flow rate. Since the outlet area of variant V2 is smaller as compared to variant V1 and V3, the mean velocity at the outlet is 55.7 mm/s for V2. This value is more than doubled as compared to variants V1 and V3 where the mean velocity at the outlet is 24.8 mm/s. This higher outlet velocity results in an about doubled velocity of the front meniscus which is about 60 mm/s for variant V2. Furthermore, no bubble pinch-off is observed for this case. However, during the late stage of the simulation the results for variant V2 are most probably influenced by the boundary conditions at the outlet (Figure 12 h). A pinch-off of the bubble may be potentially observed for a computational domain where H_2 is increased. However, this issue is not investigated here.

For variant V2, the phase distribution in the upper pipe visually approaches the Bretherton problem. The capillary number based on the velocity of the front meniscus is about 0.001 for this case. This corresponds to a liquid film thickness in the Bretherton problem of about 28 μm according to Eq. (9). The actual film thickness in the present simulation is about 680 μm (Figure 12 f-h) and thus about a factor of 25 larger. This large discrepancy can be attributed to the grid resolution (h = 30 μm) and the capillary width (ε = 40 μm), both being larger than 28 μm. We expect that simulations where h and ε are reduced by say a factor of 5, will yield a much thinner liquid film for this case. Since such simulations are very time consuming they are not considered here. The difficulties of diffuse interface methods in computing Taylor flow at capillary numbers $Ca_B < 2 \cdot 10^{-3}$ are also emphasized in [52].

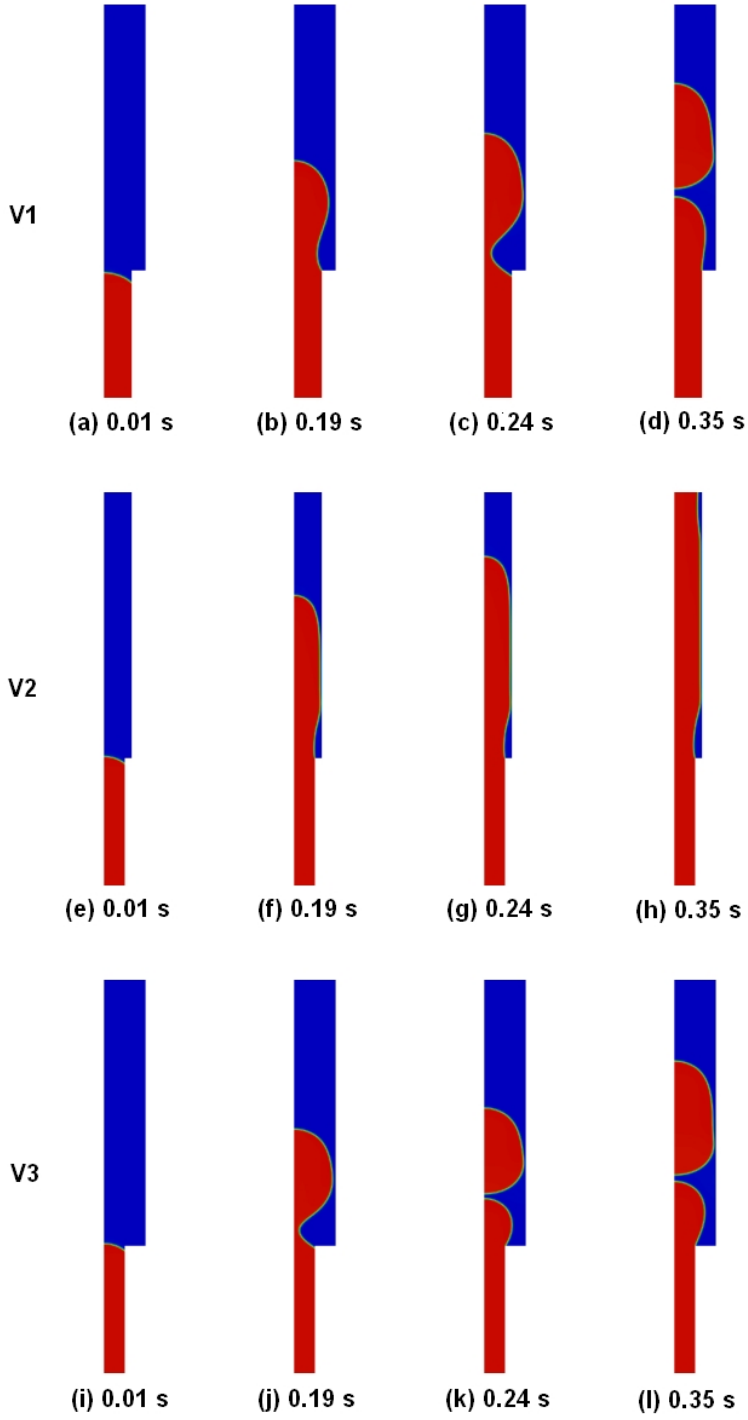

Figure 12: 2D axisymmetric results for variants V1, V2 and V3. The simulations have the same grid size and parameters (h = 30 µm, ε = 40 µm, N_C = 6, $M = 16\times10^{-10}$ m^{3}s/kg)

4.2.3 Variation of Inclination Angle

To study the influence of the inclination angle in the transition region between both pipes, we consider further geometrical variants V4, V5 and V6 where α is varied while both tube diameters are fixed (D_1 = 3 mm, D_2 = 6 mm). The simulation results are displayed in Figure 13. For both the variants V5 and V6, the contact line first advances on the inclined transition region (Figure 13 f and j) but then recedes (Figure 13 g and k) so that gas pinch-off is about to happen (Figure 13 h and l). By comparison, the contact line pinning does not arise for V4 and the stratified gas-liquid interface is passing smoothly over the entire cone region (Figure 13b). As a result, no pinch-off occurs for this variant. The simulation for case V4 is stopped at 0.3 s, since it is already clear that the interface will retract without bubble formation. These simulation results suggest that a critical inclination angle for gas pinch-off exists being in the range between $\alpha = 35°$ (V4) and $\alpha = 50°$ (V5). Yet, further attempts to identify the critical angle are not pursued in this contribution.

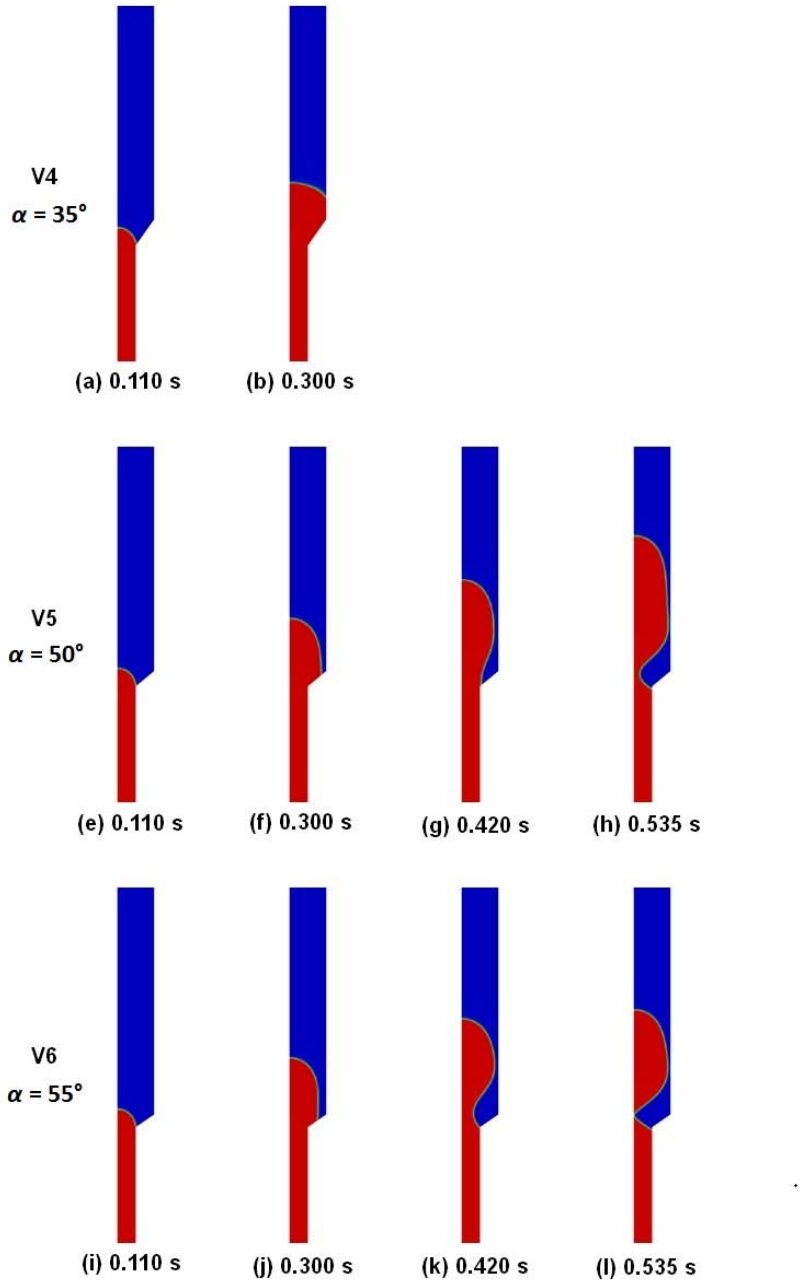

Figure 13: 2D axisymmetric results for geometrical variants V4, V5 and V6, where the transition inclination angle is varied from $\alpha = 35°$, 50° to 55°. The simulations have the same grid size and parameters ($h = 40$ μm, $\varepsilon = 40$ μm, $Cn = 0.013$, $N_C = 4$, $M = 16\times10^{-10}$ m^{3}s/kg)

5 Summary and Outlook

In this paper, we studied the draining of urea-water-solution by back suction through a generalized geometry consisting of two connected concentric pipes of different diameter and the associated potential gas bubble formation by interface-resolving numerical simulations with a phase field method. For obtaining reliable numerical results, the following computational guidelines are proposed. For 3D simulations, it is of importance to use a mesh aligned with the tube wall. If a non-aligned mesh has to be used (e.g., in some complex geometry where the generation of an aligned mesh is rather challenging), it is highly recommended to use surface normal gradient correction to handle the mesh non-orthogonality near the wall. This is of special relevance for the phase field method where the wall wettability is accounted for by the gradient of the order parameter. For 2D axisymmetric simulations, grid independence is achieved, provided the diffuse interface region is resolved by at minimum six mesh cells.

The investigations of the influence of the geometry on the liquid draining and bubble formation process indicate that decreasing the diameter ratio between the larger upper and smaller lower pipe toward unity may delay bubble formation, while reducing the inclination angle can completely suppress bubble formation even for a diameter ratio of two. These results suggest that geometrical modification is an effective way to control liquid draining while preventing gas bubble formation. The findings of the present study may be helpful for future engineering CFD-based design and optimization studies for real technical geometries.

For a detailed validation of the present numerical model, experiments on the liquid draining process and bubble formation within the considered sample geometry would be highly useful. Concerning the physics of the draining process, uncovering the influences of material properties – such as wall wettability and roughness – on the critical cone inclination angle below which bubble formation is suppressed would be of interest. Furthermore, a potential relation between the maximum inclination angle α where no bubbles are emitted and the flow rate would be useful for the conception of the design.

Acknowledgments

X.C. and O.D. acknowledge the support by the Deutsche Forschungsgemeinschaft through SFB/Transregio 150 project B05. H.M. acknowledges the support by the Deutsche Forschungsgemeinschaft through SFB 1194 project B02.

Conflict of Interest: On behalf of all authors, the corresponding author states that there is no conflict of interest.

References

1. Koebel, M., Elsener, M., Marti, T.: NO_x-reduction in diesel exhaust gas with urea and selective catalytic reduction. Combust. Sci. Technol. **121** (1-6), 85-102 (1996)
2. Koebel, M., Elsener, M., Kleemann, M.: Urea-SCR: a promising technique to reduce NO_x emissions from automotive diesel engines. Catal. Today **59** (3-4), 335-345 (2000)
3. Birkhold, F., Meingast, U., Wassermann, P., Deutschmann, O.: Analysis of the Injection of Urea-Water-Solution for Automotive SCR $DeNO_x$-Systems: Modeling of Two-Phase Flow and Spray/Wall-Interaction. SAE Technical Paper 2006-01-0643 (2006)
4. Birkhold, F., Meingast, U., Wassermann, P., Deutschmann, O.: Modeling and simulation of the injection of urea-water-solution for automotive SCR $DeNO_x$-systems. Appl. Catal. B-Environ. **70** (1-4), 119-127 (2007)
5. Deutschmann, O., Grunwaldt, J.D.: Exhaust Gas Aftertreatment in Mobile Systems: Status, Challenges, and Perspectives. Chem. Ing. Tech. **85** (5), 595-617 (2013)
6. Brack, W., Heine, B., Birkhold, F., Kruse, M., Schoch, G., Tischer, S., Deutschmann, O.: Kinetic modeling of urea decomposition based on systematic thermogravimetric analyses of urea and its most important by-products. Chem. Eng. Sci. **106**, 1-8 (2014)
7. Brack, W., Heine, B., Birkhold, F., Kruse, M., Deutschmann, O.: Formation of Urea-Based Deposits in an Exhaust System: Numerical Predictions and Experimental Observations on a Hot Gas Test Bench. Emis. Contr. Sci. Technol. **2** (3), 115-123 (2016)
8. Nova, I., Tronconi, E.: Urea-SCR technology for deNOx after treatment of diesel exhausts. Fundamental and applied catalysis. Springer, New York (2014).
9. Nishioka, A., Sukegawa, Y., Katogi, K., Mamada, H., Kowatari, T., Mukai, T., Yokota, H.: A Study of a New Aftertreatment System (2): Control of Urea Solution Spray for Urea-SCR. SAE Technical Paper 2006-01-0644 (2006)
10. Stola, F., De Cesare, M., Lacchini, L., Cavina, N., Sohal, S.: Diesel Exhaust Fluid (DEF) Supply System Modelling for Control and Diagnosis Applications. SAE Technical Paper 2015-26-0090 (2015)
11. Shost, M., Noetzel, J., Wu, M.-C., Sugiarto, T., Bordewyk, T., Fulks, G., Fisher, G.B.: Monitoring, Feedback and Control of Urea SCR Dosing Systems for NOx Reduction: Utilizing an Embedded Model and Ammonia Sensing. SAE Technical Paper 2008-01-1325 (2008)

12. Kowatari, T., Hamada, Y., Amou, K., Hamada, I., Funabashi, H., Takakura, T., Nakagome, K.: A Study of a New Aftertreatment System (1): A New Dosing Device for Enhancing Low Temperature Performance of Urea-SCR. SAE Technical Paper 2006-01-0642 (2006)
13. Hüthwohl, G., Dolenec, S.: A new Approach in AdBlue Dosing to Improve Performance and Durability of SCR Systems for the Use in Passenger Cars up to Heavy Duty Vehicles. SAE Technical Paper 2011-01-2095 (2011)
14. Aus der Wiesche, S.: Numerical heat transfer and thermal engineering of AdBlue (SCR) tanks for combustion engine emission reduction. Appl. Therm. Eng. **27** (11-12), 1790-1798 (2007)
15. Choi, B., Woo, S.M.: Numerical analysis of the optimum heating pipe to melt frozen urea-water-solution of a diesel urea-SCR system. Appl. Therm. Eng. **89**, 860-870 (2015)
16. Kruse, C., Nagel, T., Schepers, S., Hodgson, J.: Method for draining a delivery unit for liquid additive, delivery unit and motor vehicle having a delivery unit. Patent EP 2844852 B1 (US 2015/0033712 A1) (2015)
17. Eriksson, L., Carlsson, U.: Method pertaining to air removal from a liquid supply system and a liquid supply system. Patent WO 2011/162693 A1 (2011)
18. Anderson, D.M., McFadden, G.B., Wheeler, A.A.: Diffuse-interface methods in fluid mechanics. Annu. Rev. Fluid Mech. **30**, 139-165 (1998)
19. Marschall, H., Cai, X., Wörner, M., Deutschmann, O. Development of Phase Field Methods using OpenFOAM® - Part I: Method Development and Implementation. In: 10th International OpenFOAM® Workshop, Ann Arbor, Michigan, USA, 2015.
20. Marschall, H., Cai, X., Wörner, M., Deutschmann, O.: Conservative finite volume discretization of the two-phase Navier-Stokes Cahn-Hilliard and Allen-Cahn equations on general grids with applications to dynamic wetting. In preparation (2017)
21. Cai, X., Marschall, H., Wörner, M., Deutschmann, O.: Numerical Simulation of Wetting Phenomena with a Phase-Field Method Using OpenFOAM®. Chem. Eng. Technol. **38** (11), 1985-1992 (2015)
22. Cai, X., Wörner, M., Marschall, H., Deutschmann, O.: Numerical study on the wettability dependent interaction of a rising bubble with a periodic open cellular structure. Catal. Today **273**, 151-160 (2016)
23. Jacqmin, D.: Calculation of Two-Phase Navier-Stokes Flows Using Phase-Field Modeling. J. Comput. Phys. **155** (1), 96-127 (1999)
24. Weller, H.G.: A new approach to VOF-based interface capturing methods for incompressible and compressible flow, Tech. Rep. TR/HGW/07, OpenCFD Ltd., (2006)
25. Wörner, M.: Numerical modeling of multiphase flows in microfluidics and micro process engineering: a review of methods and applications. Microfluid. Nanofluid. **12** (6), 841-886 (2012)
26. Rowlinson, J.S.: Translation of J.D. Van der Waals "The Thermodynamic Theory of Capillarity under the Hypothesis of a Continuous Variation of Density". J. Stat. Phys. **20** (2), 197-244 (1979)
27. Bray, A.J.: Theory of Phase-Ordering Kinetics. Adv. Phys. **43** (3), 357-459 (1994)
28. Yue, P.T., Zhou, C.F., Feng, J.J.: Sharp-interface limit of the Cahn-Hilliard model for moving contact lines. J. Fluid Mech. **645**, 279-294 (2010)

29. Villanueva, W., Amberg, G.: Some generic capillary-driven flows. Int. J. Multiphase Flow **32** (9), 1072-1086 (2006)
30. Kusumaatmaja, H., Hemingway, E.J., Fielding, S.M.: Moving contact line dynamics: from diffuse to sharp interfaces. J. Fluid Mech. **788**, 209-227 (2016)
31. Cox, R.G.: The Dynamics of the Spreading of Liquids on a Solid-Surface .1. Viscous-Flow. J. Fluid Mech. **168**, 169-194 (1986)
32. Kim, J.: A continuous surface tension force formulation for diffuse-interface models. J. Comput. Phys. **204** (2), 784-804 (2005)
33. He, Q.W., Kasagi, N.: Phase-Field simulation of small capillary-number two-phase flow in a microtube. Fluid Dyn. Res. **40** (7-8), 497-509 (2008)
34. Jasak, H., Nilsson, H., Rusche, H., Beaudoin, M., Gschaider, B.: Release Notes for FOAM-Extend-3.2, https://sourceforge.net/p/foam-extend/foam-extend-3.2/ci/master/tree/ReleaseNotes.txt, The FOAM-Extend project (2015)
35. Ding, H., Spelt, P.D.M., Shu, C.: Diffuse interface model for incompressible two-phase flows with large density ratios. J. Comput. Phys. **226** (2), 2078-2095 (2007)
36. Abels, H., Garcke, H., Grün, G.: Thermodynamically Consistent, Frame Indifferent Diffuse Interface Models for Incompressible Two-Phase Flows with Different Densities. Math. Mod. Meth. Appl. S. **22** (3), 1150013 (2012)
37. Greenshields, C.: OpenFOAM User Guide, http://foam.sourceforge.net/docs/Guides-a4/UserGuide.pdf, CFD Direct Ltd. (2015)
38. Khatavkar, V.V., Anderson, P.D., Meijer, H.E.H.: Capillary spreading of a droplet in the partially wetting regime using a diffuse-interface model. J. Fluid Mech. **572**, 367-387 (2007)
39. Ding, H., Li, E.Q., Zhang, F.H., Sui, Y., Spelt, P.D.M., Thoroddsen, S.T.: Propagation of capillary waves and ejection of small droplets in rapid droplet spreading. J. Fluid Mech. **697**, 92-114 (2012)
40. Yue, P., Feng, J.J.: Can diffuse-interface models quantitatively describe moving contact lines? Eur. Phys. J. Spec. Top. **197** (1), 37-46 (2011)
41. Young, W.B.: Analysis of capillary flows in non-uniform cross-sectional capillaries. Colloids Surf., A **234** (1-3), 123-128 (2004)
42. Liou, W.W., Peng, Y.Q., Parker, P.E.: Analytical modeling of capillary flow in tubes of nonuniform cross section. J. Colloid Interface Sci. **333** (1), 389-399 (2009)
43. Berthier, J., Gosselin, D., Pham, A., Boizot, F., Delapierre, G., Belgacem, N., Chaussy, D.: Spontaneous capillary flows in piecewise varying cross section microchannels. Sens. Actuators, B **223**, 868-877 (2016)
44. Erickson, D., Li, D., Park, C.B.: Numerical simulations of capillary-driven flows in nonuniform cross-sectional capillaries. J. Colloid Interface Sci. **250** (2), 422-430 (2002)
45. Mehrabian, H., Gao, P., Feng, J.J.: Wicking flow through microchannels. Phys. Fluids **23** (12), 122108 (2011)
46. Figliuzzi, B., Buie, C.R.: Rise in optimized capillary channels. J. Fluid Mech. **731**, 142-161 (2013)
47. Yue, P., Zhou, C., Feng, J.J.: Spontaneous shrinkage of drops and mass conservation in phase-field simulations. J. Comput. Phys. **223** (1), 1-9 (2007)

48. Bretherton, F.P.: The Motion of Long Bubbles in Tubes. J. Fluid Mech. **10** (2), 166-188 (1961)

49. Bai, F., He, X., Yang, X., Zhou, R., Wang, C.: Three dimensional phase-field investigation of droplet formation in microfluidic flow focusing devices with experimental validation. Int. J. Multiphase Flow **93**, 130-141 (2017)

50. Jamialahmadi, M., Zehtaban, M.R., Müller-Steinhagen, H., Sarrafi, A., Smith, J.M.: Study of Bubble Formation Under Constant Flow Conditions. Chem. Eng. Res. Des. **79** (5), 523-532 (2001)

51. Gerlach, D., Alleborn, N., Buwa, V., Durst, F.: Numerical simulation of periodic bubble formation at a submerged orifice with constant gas flow rate. Chem. Eng. Sci. **62** (7), 2109-2125 (2007)

52. Aland, S., Boden, S., Hahn, A., Klingbeil, F., Weismann, M., Weller, S.: Quantitative comparison of Taylor flow simulations based on sharp-interface and diffuse-interface models. Int. J. Numer. Methods Fluids **73** (4), 344-361 (2013)